FINITE VOLUME NUMERICAL METHODS FOR AEROHEATING RATE CALCULATIONS FROM INFRARED THERMOGRAPHIC DATA

Kamran Daryabeigi,[*] Scott A. Berry,[+] Thomas J. Horvath,[‡] and Robert J. Nowak[§]

NASA Langley Research Center, Hampton, Virginia 23681

Abstract

The use of multi-dimensional finite volume heat conduction techniques for calculating aeroheating rates from measured global surface temperatures on hypersonic wind tunnel models was investigated. Both direct and inverse finite volume techniques were investigated and compared with the standard one-dimensional semi-infinite technique. Global transient surface temperatures were measured using an infrared thermographic technique on a 0.333-scale model of the Hyper-X forebody in the NASA Langley Research Center 20-Inch Mach 6 Air tunnel. In these tests the effectiveness of vortices generated via gas injection for initiating hypersonic transition on the Hyper-X forebody was investigated. An array of streamwise-orientated heating striations was generated and visualized downstream of the gas injection sites. In regions without significant spatial temperature gradients, one-dimensional techniques provided accurate aeroheating rates. In regions with sharp temperature gradients caused by striation patterns multi-

---

[*] Aerospace Technologist, Metal and Thermal Structures Branch, MS 396, Senior Member AIAA
[+] Aerospace Technologist, Aerothermodynamics Branch, MS 408A,
[‡] Aerospace Technologist, Aerothermodynamics Branch, MS 408A
[§] Research Scientist, Aerothermodynamics Branch, MS 408A, Member AIAA

dimensional heat transfer techniques were necessary to obtain more accurate heating rates. The use of the one-dimensional technique resulted in differences of ±20% in the calculated heating rates compared to 2-D analysis because it did not account for lateral heat conduction in the model.

Nomenclature

c	specific heat, J/kg/K
Fo	Fourier number
h	enthalpy-based heat transfer coefficient, kg/m^2/s
h_{ref}	reference heat transfer coefficient, kg/m^2/s
H	enthalpy, J/kg
k	thermal conductivity, W/m/K
L	length, m
L_x	length of 1st Macor insert, m
L_y	width of 1st Macor insert, m
L_z	thickness of Macor inserts, m
M	Mach number
$\hat{n}$	unit normal vector
q''	heat flux, W/m^2
Re	Reynolds Number
T	temperature, K
T_o	initial (pre-run) temperature, K

t	run time (measured from initiation of model injection), s
t_1	time model is at test section centerline, s
t_{corr}	correction time, s
t_{eff}	effective time, s
S	sum of square of errors
x	local coordinate along model length
y	local coordinate along model width
z	local coordinate along model thickness

α	thermal diffusivity, m^2/s
β	thermal product, $\sqrt{\rho c k}$, $J/m^2/K/s^{0.5}$
ε	emittance
ρ	density, kg/m^3
σ	Stefan-Boltzmann constant, 5.668×10^{-8} $W/m^2/K^4$

Subscripts

aw	adiabatic wall condition
m	measured
p	predicted
t1	reservoir conditions
t2	stagnation conditions behind normal shock
tw	tunnel wall
w	wall condition
o	initial

∞	free-stream static condition

Acronyms

CFD	computational fluid dynamics
FV	finite volume
SI	semi-infinite

Introduction

One of the standard techniques for calculating aeroheating rates from measured transient surface temperatures on hypersonic wind tunnel models has been the one-dimensional semi-infinite solid conduction method. This method was originally developed for use with discrete temperature sensors, such as thin film resistance gages.[1] The semi-infinite technique assumes that heat does not noticeably diffuse to the back surface of the model, so that the back surface temperature does not vary with time. It is also assumed that there is no lateral heat conduction so that heat is conducted only in the direction of the model thickness from the top surface (surface exposed to aeroheating) to the back surface. This assumption is necessary when using discrete temperature sensors, since due to limitations on the number and spacing of the sensors that can be installed on the model multi-dimensional conduction cannot be considered. There are several limitations to the use of the 1-D semi-infinite method. The semi-infinite assumption is only valid for a specific time duration that is a function of model thickness and thermophysical properties. The method assumes constant thermophysical properties. Furthermore, this technique is not suitable for regions with sharp temperature gradients across the surface, because lateral heat conduction may be significant compared to through-the-thickness heat conduction.

To overcome limitations on the number of discrete sensors that can be installed on models, optical techniques such as infrared and phosphor thermal imaging have been utilized for providing global aeroheating data on hypersonic wind tunnel models. The phosphor thermography technique is routinely used for hypersonic wind tunnel aeroheating measurements.[2] The accuracy of infrared thermal imaging for transient surface temperature measurements on a flat plate model in subsonic flow has been evaluated by comparison with surface-mounted thermocouples.[3] This technique has been used for aeroheating calculations on hypersonic wind tunnel models,[4, 5] and for in-flight surface temperature measurements on the Shuttle Orbiter.[6, 7] The 1-D semi-infinite technique is the standard method used with thermal imaging techniques, even though the availability of whole-field surface temperature distributions lends itself to using numerical multi-dimensional thermal analysis. The 1-D semi-infinite method yields a simple analytical solution,[8] while multi-dimensional solid conduction analysis requires numerical thermal analysis software and complete modeling of the geometry of the wind tunnel model. The present study is an attempt to investigate the use of multi-dimensional heat conduction models with global thermal data as the next level of data reduction methods.

Numerical techniques have previously been used with discrete sensors to overcome some of the 1-D semi-infinite limitations. The 1-D finite volume technique has been used for calculating aeroheating rates from discrete sensors on hypersonic wind tunnel models.[9, 10] This technique numerically solves the governing diffusion equation using the measured temperatures on the top surface and assuming an adiabatic back face boundary condition. The main advantage of this technique is that it can use temperature dependent material properties and it does not have the time limitation validity issues associated with the semi-infinite technique. An inverse 2-D finite element numerical technique has been used in conjunction with temperature measurements from a linear array of closely spaced thin film gages to obtain heating rate distributions in the region of shock impingement on a cylinder in Mach 6 flow.[11] This technique resulted in higher peak heating rate predictions at shock impingement locations, but the accuracy of the technique could not be determined due to limitations on the number of sensors used.

In order to investigate multi-dimensional finite volume heat conduction techniques with global thermal imaging data, a series of runs were conducted as a subset of an overall experimental program for evaluating gas injection for tripping the boundary layer on a 0.333-scale Hyper-X forebody model. This tripping mechanism produced an array of streamwise orientated heating striations downstream of the gas injection sites. Various solid trip configurations had previously been investigated on this 0.333- scale Hyper-X forebody model.[12] The overall test program was a comprehensive study to investigate the effectiveness of gas injection for hypersonic boundary layer transition and included more than 80 wind tunnel runs. It used phosphor thermography for aeroheating measurements and included oil flow visualization runs. The runs reported here were a small subset of the overall test program and concentrated on evaluation of multi-dimensional solid conduction numerical methods in conjunction with infrared thermographic techniques to study the striation heating downstream of the gas injection sites.

The main objective of this investigation was to compare 1-D and multi-dimensional finite volume methods for predicting heating rates, especially in regions with significant spatial temperature gradients.

Experimental Methodology

Test Facility

Aeroheating data were obtained on a 0.333-scale Hyper-X forebody model in the 20-Inch Mach 6 Air Tunnel of the NASA Langley Research Center Aerothermodynamics Laboratory.[13] This tunnel is a conventional blowdown tunnel with a 0.521 m × 0.508 m (20.5 × 20 in.) test section, and uses a two-dimensional contoured nozzle to provide a nominal freestream Mach number of six. The tunnel uses dried, heated, filtered air as the test gas. A detailed description of the facility and its associated instrumentation is found in Ref. 13. Typical operating conditions for the tunnel are stagnation pressures of 0.21-3.45 MPa, stagnation temperatures of 483-533 K, and free stream unit Reynolds numbers of 1.6×10^6/m-25.6×10^6/m. A bottom-mounted model injection system inserts models from a sheltered position to the tunnel centerline in approximately 1-2 seconds, and typical duration of aeroheating tests in this facility is 5–10 seconds.

Model

A photograph of the 0.333-scale Hyper-X forebody model is shown in Fig. 1. This model is described in detail in Ref. 12, and was previously used for comparing the effectiveness of various hypersonic boundary-layer trip devices.[12] The windward forebody model consisted of three flat ramps that provided a series of discrete nonisentropic flow compression surfaces simulating the engine external inlet ramps. The model was tested at 2° angle of attack, and the first, second, and third ramps provided additional compressions of 2.5°, 5.5°, and 3°, respectively.

The 71.12-cm long forebody model was built from aluminum and had a detachable stainless-steel leading edge (nose radius of 0.254 mm) and interchangeable measurement surface inserts. The length of the leading edge was 12.7-cm, while the trip station was 18.84-cm from the model leading edge. The trip insert plates consisted of several stainless steel inserts with various orifice shapes and spacing for gas injection into the flow in order to trip the boundary layer. The specific trip insert plate used for this report consisted of a single row of 17 orifices, 0.25-mm in diameter with a 3.18-mm spacing. The remaining flat ramp sections were designed to accommodate either a Macor[*] or aluminum set of inserts. The Macor and aluminum inserts were used for heat transfer and flow visualization studies, respectively. The Macor inserts were 6.35-mm thick. The leading edge of the first insert plate, 10.87-cm long and 12.9-cm wide, was 20.74-cm downstream of the model leading edge. Since phosphor thermography was the main measurement system used for obtaining heating rates for the overall experimental program, the Macor substrates were coated with a 0.025-mm thick mixture of phosphors suspended in a silica-based colloidal binder. A photograph of part of the model showing the leading edge, the trip insert plate with 17 orifices for gas injection, and the first Macor insert is shown in Fig. 2.

Test Conditions

The nominal reservoir stagnation pressure and temperature for the two runs reported in the present study are presented in Table 1. The reported flow conditions were based on the measured reservoir stagnation pressures and temperatures and recent unpublished tunnel calibrations. Both runs were conducted with the model at an angle of attack of 2°. Run 70 was a baseline test without gas injection into the boundary layer, while Run 71 consisted of gas injection into the boundary layer. The total pressure of the gas injected into the boundary layer

---

[*] a machinable glass ceramic which is a registered trademark of Corning Incorporated

was measured in a manifold directly below the orifices, and was 31.2 kPa. The total pressure was used to control the penetration depth of the jets compared to the boundary layer thickness.

Test Technique

Model surface temperatures were measured using an infrared imaging system with an uncooled microbolometer-based focal plane array detector with 320 × 240 detector elements. The imager has a field of view of 24° × 18°, and is sensitive to infrared radiation emitted in the 7–12 micrometer spectral range of the electromagnetic spectrum. An eight-inch diameter zinc selenide window with anti-reflection coating to provide transmittance of 0.98 in the 7-14 micrometer spectral range was used for optical access to the test section. The measured infrared radiation is converted to actual surface temperatures using the emittance of target. Ceramic models have high emittance values and do not require any special coating for infrared thermal measurements. But the Macor inserts used in this test had already been coated with phosphor coating to obtain global thermographic phosphor data in subsequent tunnel runs. The room-temperature, total (wavelength averaged), near normal emittance of the Macor inserts with the applied surface phosphor coating was determined to be 0.88 using a heated cavity reflectometer.[14] Joints between the Macor inserts corresponding to the location of ramp angle changes (Fig. 1) were used to geometrically locate the model in image mappings. The imager produces 30 frames of images per second, while the data acquisition hardware used was only capable of real–time digital storage of approximately 5 frames per second. Surface temperatures were measured on parts of the model leading edge, the entire first Macor insert, and part of the second Macor insert, but only the data from the first Macor insert was used in this study to compare various aeroheating calculation techniques. Model surface streamlines were obtained using the oil flow technique to correlate with aeroheating results. For oil flow tests, metal inserts used on the model were spray painted with black paint to enhance contrast with the white-pigmented oil, and surface streamlines were recorded using a conventional video camera.[12]

Test Procedure

In order to compare results from the multidimensional finite volume heat conduction technique with the standard semi-infinite technique, a "pre-run" image was obtained, which is the standard procedure used for data reduction using the semi-infinite technique with global optical techniques.[2] This procedure consisted of injecting the model into the test section just prior to establishing tunnel flow and obtaining a "pre-run" image of initial surface temperature distribution across the model. Then the model was retracted. The tunnel underwent to a "pre-heat" cycle where the gas in the stagnation chamber was heated to the desired total temperature. After the flow was established, the model was injected into the test section, and the start of the injection process triggered the infrared imaging digital recording process at 0.2 s intervals. Fig. 3 shows a schematic of the test set-up. As the actual size of the target (first Macor insert) image varied during the model injection process, a mapping process was utilized using linear interpolation of data to map images obtained during injection process to the final image size (constant image size after model had reached the stationary position in the test section).

Solution Techniques

1-D Semi-Infinite Method

The standard 1-D semi-infinite data reduction method is used in this study as a basis of comparison with numerical methods. While the standard 1-D semi-infinite solid conduction formulation with specified surface temperature boundary condition is typically used with discrete sensors, it is not utilized with global optical techniques. This is primarily due to two factors.

Continuous digital recording of whole images (as high as 512 by 512 pixels) requires significant image processing hardware speed and storage space. Furthermore, mapping of temperature fields is required during the injection process because image size of the target varies till the model reaches its stationary position at the test section centerline. A simple standard technique has been developed and evaluated which requires storage of only two images, one before the test for initial condition (referred to as "pre-run") and one after the model has reached the centerline.[2] Then the semi-infinite solid conduction formulation with convective boundary condition is used.[2] The governing equation is the constant property 1-D heat conduction equation, with an enthalpy-based convective boundary condition

$$-k\frac{\partial T}{\partial z}(0,t) = h\left[H_{aw} - H_w(t)\right] \tag{1}$$

H_{aw} is the adiabatic wall enthalpy assumed to be equal to the total enthalpy (H_{t1} in Table 1), and H_w is the wall enthalpy evaluated at wall temperature [$T_w = T(0,t)$]. The analytical solution is

$$T(z,t) = T_0 + \left[H_{aw}\frac{T(0,t)}{H_w(t)} - T_0\right]\left[erfc(\eta) - e^{\frac{hH_w z}{T(0,t)k} + \lambda^2} erfc(\lambda + \eta)\right] \tag{2}$$

where T_0 is the initial temperature , typically obtained from the "pre-run" image, and

$$\eta = \frac{z}{2\sqrt{\alpha t}} \tag{3.a}$$

$$\lambda = \frac{hH_w(t)\sqrt{t}}{T(0,t)\beta} \tag{3.b}$$

$$\beta = \sqrt{\rho c k} \tag{3.c}$$

where *erfc* is the complimentary error function. At the surface (*z=0*), the solution reduces to

$$\frac{T(0,t)-T_o}{\frac{H_{aw}}{H_w(t)}T(0,t)-T_0} = 1 - e^{\lambda^2}\, erfc\lambda \tag{4}$$

The measured surface temperature is used in Eq. (4) to solve for λ, which then yields the heat transfer coefficient, *h,* from Eq. (3.b). Since the formulation is for constant thermophysical properties, calculations are made using temperature-averaged properties.[2] The above calculations are performed for every point (pixel) in the image, assuming that heat transfer is only in the direction of model thickness. All that is needed to compute heat transfer coefficient distributions over the model is the initial surface temperature distribution, T_0 (typically from pre-run), and temperature distribution at one instant of time after the model has reached the test section centerline, T(0,t). This technique assumes that the heat transfer coefficient distribution is time invariant. This assumption is not valid when the model is traversing through the test section's boundary layer. In order to overcome this difficulty, the injection process is modeled as a delayed step heating, with the delay in the step corresponding to the time when the model has traversed halfway through the tunnel boundary layer.[2] The time it takes from the initiation of the injection process until the model traverses halfway through the tunnel boundary layer edge is referred to as the "correction time", t_{corr}, and is subtracted from the run time to obtain an effective time to be used in the above equations[2]

$$t_{eff} = t - t_{corr} \tag{5}$$

where *t* is the actual run time which is triggered when the injection system first starts to move. The calculation of t_{corr} is described in detail in Ref. 2. Then t_{eff} is used instead of t in Eqs. (2-4). This technique has been validated by aeroheating calculations on a 50.8-mm diameter hemisphere in Mach 10 flow,[2] and has been applied to typical blunt body configurations such as X-34[2] and X-33.[15]

Even though the technique yields a simple analytical solution, it has a few shortcomings. First, it assumes that there is no lateral conduction, and uses constant thermophysical properties. Second, the boundary condition used in Eq. (1) assumes that all the aerodynamic heating at the surface is simply balanced by heat conduction into the model. A more realistic boundary condition would assume that the impinging aerodynamic heating is balanced by both heat conduction into the model and radiation from the model surface to the tunnel test section walls. The radiation boundary condition becomes more significant with rising model surface temperatures. But a simple analytical solution cannot be obtained if radiation heat transfer is included in the energy balance at the surface. Third, the technique is based on obtaining a "pre-run" image for initial temperature distribution, T_0, as described previously in the test procedure section. The pre-heating of the gas in the tunnel stagnation chamber also causes heating in the test section and, therefore, some heating of the model may occur just prior to injection of the model into the test section. For the solutions obtained using the semi-infinite technique in this study differences resulting from use of "pre-run" image and image at the beginning of injection process ($t = 0$ s) are investigated. Furthermore, the effect of the effective time approach is also studied.

<u>Finite Volume Numerical Technique</u>

In the present study, the differences resulting from 1, 2 and 3-D finite volume treatment of data will be studied. Full-field surface temperatures were measured using infrared imaging, and the corresponding full-field surface heating rates were calculated using finite volume techniques. As mentioned previously only the data from the first Macor insert are discussed in this study in order to simplify geometrical considerations and concentrate on the basic aeroheating calculation issues. Referring to Fig. 4 for local coordinate system and geometrical definitions, the governing 3-D diffusion equation and initial and boundary conditions used for the Macor insert were

$$\rho \mathrm{c}\frac{\partial T}{\partial \mathrm{t}}=\frac{\partial}{\partial x}(k\frac{\partial T}{\partial \mathrm{x}})+\frac{\partial}{\partial y}(k\frac{\partial T}{\partial \mathrm{y}})+\frac{\partial}{\partial z}(k\frac{\partial T}{\partial \mathrm{z}}) \tag{6.a}$$

$$T(x,y,z,0)=g(x,y,z) \tag{6.b}$$

$$T(x,y,0,t)=f(x,y,t) \tag{6.c}$$

while, on all other boundaries:

$$\nabla \mathrm{T}.\hat{\mathrm{n}}=0 \tag{6.d}$$

For simplicity it was assumed that adiabatic boundary conditions existed at the edges of the Macor insert (y = 0, $y = L_y$, x = 0, and $x = L_x$), Eq. (6.c). It was assumed that the model back face ($z = L_z$) is adiabatic [Eq. (6.d)], while the top surface has a specified transient temperature distribution, f(x,y,t), measured using the optical thermographic technique [Eq. (6.c)]. The backface adiabatic assumption is certainly valid during the time the semi-infinite assumption is valid. Furthermore, after the back face temperature begins to rise, the heat losses from the back face are typically low enough that the assumption of an adiabatic condition may not introduce large errors. For the direct finite volume technique, the initial temperature distribution for Eq. (6.b) was obtained from the image at the beginning of injection process (t = 0 s), assuming uniform initial temperature distribution through the thickness at each pixel location.

The governing equations for the 2-D and 1-D finite volume techniques are subsets of the set of equations provided in Eqs. (6.a)-(6.d). For the 1-D case the dependence on *x* and *y* coordinates and the corresponding boundary conditions in these directions are eliminated. For the 2-D case the dependence on either *x or y* coordinate and the corresponding boundary conditions in these directions are eliminated. The solution to this set of equations constitutes the direct solution method. In the present study, the equations were solved using a finite volume numerical method with variable thermophysical properties. The transient problem was solved using unconditionally stable implicit time-marching techniques:[16] Crank Nicholson method for the 1-D case and Alternating-Direction Implicit (ADI) method for the 2-D and 3-D cases. The governing equations and the derivative boundary conditions were formulated such that second-order accuracy could be achieved with truncation errors on the order of Δt^2 and $\Delta \mathbf{x}^2$, where Δt and $\Delta \mathbf{x}$ are the time step and spatial nodal spacing, respectively. For the results reported here 21 nodes were used in the z-direction, and 128 by 159 nodes in the y and x directions, respectively. The latter was dictated by the number of infrared image pixels across the top surface of the first Macor insert. Solutions obtained using 51 and 21 nodes in the z direction were similar, thus verifying that the through thickness nodal spacing used was sufficient. The time step used was dictated by the digital storage interval of infrared images, which was approximately 0.2 s. Upon numerical solution of the governing equations, the convective heat transfer coefficient, h, was calculated at each instant of time from conservation of energy for the surface volume elements:

$$-k\frac{\Delta T}{\Delta z}(x,y,0,t)+\rho c\Delta z\frac{\Delta T}{\Delta t}+\varepsilon\sigma\left[T^4(x,y,0,t)-T_{tw}^4\right]=h(x,y,t)[H_{aw}-H_w(x,y,t)] \qquad (6.e)$$

Δz is the thickness of the control volume around the node at the surface. This energy balance states that the convective heating is balanced by heat conduction into model, heat storage in the surface volume element and heat radiated to the surroundings. The standard boundary condition definition typically neglects the second and third terms on the right hand side of the equation. The second term represents energy storage at the model surface and is necessary for the energy balance in transient heating conditions. The third term on the right hand side governs radiation heat transfer from the model to the tunnel test section walls and boundaries.[17] The radiation heat loss from the model is not typically included in the semi-infinite technique, because then a simple analytical solution cannot be obtained. But the actual energy balance on the surface should include this radiation heat loss. The magnitude of this radiation heat loss is smaller for slender bodies at low heating rates, but increases with blunt bodies and tests at higher heating rates where the model surface temperature may be significantly higher than the test section walls.

In the inverse method, it is assumed that the surface is exposed to a time invariant but spatially variant heat transfer coefficient. Therefore, Eq. (6.e) is used as the boundary condition at the surface z = 0, while adiabatic boundary conditions are assumed for all the other boundaries. Because the heat transfer coefficients in Eq. (6.e) are unknown, the conjugate gradient method for nonlinear parameter estimation[18] was utilized to estimate their values. This technique is an iterative numerical scheme where a distribution of heat transfer coefficients, h(x,y), is assumed; the numerical solution to the equation using this boundary condition is marched in time and surface temperature distributions are calculated. The comparison of measured and predicted transient surface temperatures over the test interval and the Jacobian matrix representing the derivatives of surface temperatures with respect to the heat transfer coefficients are used to develop better estimates of h(x,y). This iterative procedure is based on the minimization of the ordinary least squares norm given by

$$S = \sum \left[T_m(x, y, 0, t) - T_p(x, y, 0, t) \right]^2 \tag{7}$$

where T_m and T_p are measured and predicted surface temperatures, respectively. The 1-D inverse method required estimating one heat transfer coefficient at each measurement point on the image in an uncoupled manner. The 2-D and 3-D inverse methods required simultaneous estimation of either a vector of heat transfer coefficient along a specific axis, or an array of heat transfer coefficients over the entire image, respectively. The computational effort increases tremendously as analysis is extended from 2-D to 3-D. In their 3-D inverse method for calculating aeroheating rates form thermography data, Smith and Scott[19] found it necessary to divide the geometry into several patches, which were solved separately and then combined to obtain the full solution. As discussed in the subsequent presentation of results, it was found that 2-D inverse technique was sufficient for the present study.

For the inverse finite volume method, the governing conservation of energy equation, Eq. (6.a.) was solved for time $t \geq t_1$, with $t_1$corresponding to time when the model had reached the test section centerline. The initial temperature distribution at time t_1 was

$$T\left(x, y, x, t_1\right) = g_1\left(x, y, z\right) \tag{8}$$

This initial temperature distribution was not known for $z > 0$, and the z variation was approximated at each pixel location by the analytical solution of 1-D semi-infinite conduction model, Eq. (2), at time t_1. The temperature distribution from the image obtained at $t = 0$ seconds was used instead of “pre-run” data for T_0 in this equation. Any errors in the initial temperature distribution given in Eq. (8) will be corrected after a few time steps of the numerical solution due to the diffusive nature of heat conduction. This initial through-the-thickness temperature distribution could have also been obtained from the direct finite volume method.

Uncertainty Analysis

A detailed uncertainty analysis[20] was performed to obtain uncertainty estimates for the calculated heat transfer coefficients. The total uncertainty is the sum of the bias error and the precision error. It was assumed that the sources of bias uncertainty were the bias error in temperature measurement and the uncertainty in the thermophysical properties of the model material. The only source of precision error was assumed to be the random error in temperature measurement.

It was assumed that there was ±7.3% uncertainty in the thermal diffusivity and thermal conductivity data of Macor.[21] A series of in-situ calibrations were conducted at the wind tunnel by installing a blackbody radiation source in the center of the tunnel test section and measuring its temperature using the infrared imaging system through the same optical path used during actual wind tunnel testing. The bias error (difference between temperature measurements using infrared imaging and the actual blackbody radiation source) was ± 4K for the temperature range of 300- 420 K. The precision error for temperature measurement was calculated from the random noise associated with transient temperature measurements of the blackbody radiation source, and was determined to be 1.06 K for a 95% confidence interval. The overall uncertainty for the heat transfer coefficients reported in the present study was estimated[20] to be ±5.4%.

Results and Discussion

Results for the baseline run without gas injection (Run 70) are presented to compare various techniques for calculating aeroheating rates. Then the results for the run with gas injection (Run 71) are presented. Macor thermophysical properties were obtained from published results in Ref. 9. The convective heat transfer rates were non-dimensionalized with respect to a reference heat transfer coefficient, h_{ref}, corresponding to the Fay and Riddell[22] stagnation-point heating on a 101.6-mm radius sphere. Only the surface temperature and aeroheating results on the first Macor insert are presented.

Run without Gas Injection

The run without gas injection provided uniform surface temperature and aeroheating distributions across most of the surface area of the 1st Macor insert. Therefore, this run was utilized to assess the accuracy of 1-D and multi-dimensional direct and inverse finite volume methods and to compare with semi-infinite technique. The surface temperature distribution across the first Macor insert at t = 4.89 s is shown in Fig. 5. The temperatures are generally uniform across the region, with the exception of a band of lower temperatures near the intersection of the first and second Macor inserts. The adverse pressure gradient provided by the second ramp induced a local flow separation near the end of the first Macor insert, as is evident from the lower temperatures in this region. The longitudinal distribution of surface temperature distribution along the centerline of the forebody model (y/L_y=0.5) at various times is shown in Fig. 6. Data are plotted versus the non-dimensional length, x/L_x. Run time of 0 s corresponds to when the model injection was initiated. The model reached test section centerline at 1.37 s, while the run lasted 8 s. The “pre-run” data were arbitrarily set at –1 s. The lower temperatures at $x/L_x \geq 0.9$ were due to flow separation, and the temperature drop is more evident at later times. The surface temperatures rose approximately 4 K from 0 to 8 s. The “pre-run” temperatures were on the average 1.7 K cooler than at initiation of injection (0s). The standard practice in using semi-infinite solution with convective boundary condition is to assume that the “pre-run” data provide the initial temperature distribution on the model. As described previously after the “pre-run” image is obtained, the model is retracted from the test section, and the tunnel undergoes a pre-heat cycle when the gas in the stagnation chamber is pre-heated to the desired temperature. This pre-heat cycle can last for a few minutes, with hot gases going through the test section. It appears that the model in its retracted position experiences some heating and its temperature rises by 1.3 K. For testing on blunt bodies at high Reynolds numbers when the model temperature may rise significantly during the test, this initial discrepancy in temperatures may not result in large errors.

To compare various techniques for prediction of heating rates, first average temperatures and heating rates (averaged spanwise over $0 \leq y/L_y \leq 1$) at $x/L_x=0.25$ were investigated. The surface temperatures in the vicinity of this location were spatially uniform in the longitudinal direction, thus enabling comparison of various 1-D methods. The variation of spanwise-averaged temperature at this longitudinal position with time is presented in Fig. 7. Run time of 0 s corresponds to when the model injection was initiated, while "pre-run" data were arbitrarily set at –1 s. The model reached test section centerline at 1.37 s. The average temperature rose 4.4 K from 0 to 8 s, while the "pre-run" data is 1.3 K cooler than at initiation of injection (0s). The temperature then stayed almost constant during the first 0.5 s of injection time, then started rising.

The temporal variation of spanwise-averaged heating rates at $x/L_x = 0.25$ using the semi-infinite method with convective boundary condition is shown in Fig. 8. The heating rates were calculated for all the points at this longitudinal position and then averaged. Two-dimensional laminar computational fluid dynamic (CFD) solutions from Ref. (12) are also shown in the Figure. The semi-infinite heating rates were calculated using both "pre-run" and t = 0 s data as the initial temperatures, and with and without the time correction given in Eq. (5). For this test the time correction was determined to be 0.89 s. The best results were obtained using no time correction and using data at t = 0 s as the initial temperature. The calculated heating rates using the "pre-run" data overestimates the CFD results significantly, irrespective of whether time correction was used or not. Use of time correction results in overestimation of results at earlier times, while the data tend to merge at later times (approximately 8 s). The validity of the semi-infinite assumption at this later time is questionable. The semi-infinite assumption for a convective boundary condition is valid for[23]

$$Fo = \frac{\alpha t}{L_z^2} \le 0.097 \tag{9}$$

With Macor thermophysical properties at room temperature and a model thickness of 6.35 mm, the semi-infinite assumption is only valid for $t \le 4.9$ s. So, even though reducing data at later times ($t \ge 8$ s) might produce accurate results, but the basic assumption used in the analytical solution is violated. The semi-infinite results using "pre-run" data as the initial condition yielded heating rates that were within 41- 67% and 33 – 45% of CFD results in the time interval of 4 - 8 s, with t_{corr} of 0.89 and 0 s, respectively. The semi-infinite results using $t = 0$ s data as the initial condition with $t_{corr} = 0.89$s yielded heating rates that were within 9- 18% of CFD results in the time interval of 4 - 8 s, while the results with $t_{corr} = 0$ s yielded results that were within 3.1 –5.9 % of CFD predictions in the time interval of 1.37 – 8 s. Based on these results it was concluded that for accurate 1-D semi-infinite solutions on slender bodies at low heating rates, it is essential to use $t = 0$ s data for the initial condition and not to apply any time correction.

The temporal variation of spanwise-averaged heating rates at $x/L_x = 0.25$ calculated using the direct and inverse 1-D finite volume techniques is shown in Fig. 9. CFD results and semi-infinite results without time correction and using $t = 0$ s as initial condition are also shown. The direct finite volume calculations were started at 0 s and the heating rates were calculated at each instant of time when infrared surface temperature measurements had been recorded. The heating rates exhibited a sharp increase during the injection process due to rapid temperature rise when the model encountered the flow, and then sharply decreased. The calculated heating rates were within ±14 % of CFD calculations between 3 and 5.5 s time interval and then were within ±5.5 % of CFD calculations between 5.5 and 8 s time interval (the overall uncertainty of heating rate calculations using the finite volume methods in conjunction with the infrared imaging technique was ±5.4%). The inverse finite volume results were obtained for the time period between 1.37 s and 3.5 s, and the temperature distribution through the model thickness at 1.37 s was approximated by the solution of Eq. (2) from semi-infinite method assuming no time correction and t =0 s for initial condition. The inverse finite volume results provided a time-invariant solution that was within ±3.5% of CFD solution, well within the uncertainty of measurements. The use of radiation heat loss term in the energy balance at the model surface, Eq. (6.e) only made a 0.4% difference in the calculated heat transfer coefficient for the finite volume techniques. Even though the contribution of radiation loss was almost insignificant for this low heating test, this term should not be excluded for tests at higher heating rates where the model surface temperatures significantly vary from the tunnel walls, and radiation heat transfer becomes significant.

The spanwise-averaged direct finite volume results shown in Fig. 9 exhibited larger temporal noise compared to the inverse finite volume and semi-infinite results. The inverse finite volume technique results in a time-invariant heating rate at each point, while the semi-infinite results provide results that typically approach a constant value asymptotically. The direct finite volume results provide heating rates that are based on both temporal and spatial numerical derivatives of temperature, and hence are noisier.

The spanwise variation of convective heat transfer coefficients at $x/L_x = 0.25$ calculated using one, two, and three-dimensional direct finite volume formulations are presented in Fig. 10. The 2-D results were calculated at each longitudinal position across the width of the model from $y/L_y = 0$ till $y/L_y =1$, with the dependence on x coordinate and the corresponding boundary conditions in this direction eliminated. The heating results presented in the figure were obtained by temporal averaging of data between 2.58 and 3.35 s. The three sets of results coincided with each other except at the edges (y/L_y = 0 and 1), where the 2-D and 3-D results slightly varied from 1-D results due to the imposition of the adiabatic boundary conditions at the edges for the multi-dimensional formulations. This showed that in a region without significant spatial temperature gradients, such as data at x/L_x = 0.25, using 1-D analysis was sufficient.

In summary, for regions without significant spatial temperature gradients 1-D techniques are sufficient for calculating aeroheating rates, and that there was no difference between the various techniques provided that the correct initial temperature conditions were used. It was found that for the semi-infinite technique using the standard "pre-run" image data compared to the data at the beginning of injection of model in to the tunnel could results in significant errors, and that use of time correction was not necessary. Even though the 1-D semi-infinite method produced satisfactory results, but it cannot be extended to multi-dimensional cases, can not incorporate temperature varying thermophysical properties, and can not incorporate radiation heat loss from the surface which could become significant at higher surface temperatures. The finite volume techniques can easily be extended to multidimensional cases and can incorporate radiation heat loss at the surface.

Run with Gas Injection

A run was conducted with gas injection into the boundary layer for tripping the boundary layer flow. A photograph of the oil flow visualization for a run with similar flow conditions is shown in Fig. 11. The orifices for gas injection, and the streamlines corresponding to 18 vortices downstream of the gas injection sites are visible in the photograph. Each gas injection orifice produced two vortices, with the two vortices between adjacent orifices merging together, thus, producing 18 vortices for this 17-orifice configuration. A contour plot of the corresponding non-dimensionalized convective heat transfer coefficients calculated using the 1-D inverse finite volume technique is shown in Fig. 12. The traces of 18 streamwise-oriented heating striations downstream of the gas injection sites are visible in the contour plot. Higher heat transfer rates were generated in the location of the vortices. There is both streamwise and spanwise variation in the heating rates caused by the vortices. The highest heating rates appear between longitudinal locations of $0.25 \leq x/L_x \leq 0.75$. The heating results were consistent with oil flow results in a qualitative sense.

It was believed that in the vicinity of the vortices with high spatial temperature gradients 1-D heating results might not be accurate, therefore, multi-dimensional finite volume techniques were utilized. First, direct 2-D and 3-D direct finite volume techniques were compared to determine which formulation would be more appropriate for the given run conditions. The 2-D results were calculated at each longitudinal position across the width of the model by eliminating the dependence on x coordinate and the corresponding boundary conditions in this direction. The comparison of the results at the longitudinal position of $x/L_x = 0.25$ at $t = 3.02$ s is shown in Fig. 13. The heating peaks related to the 18 vortices are visible between y/L_y of 0.2 and 0.8. The heating rates at some vortex locations are as high as 4.8 times the heating rates in the undisturbed regions. Furthermore, it is seen that there is no significant difference between the heating results predicted using either the 2-D or 3-D analysis, with the root mean square difference between the two sets of results being 1%. Therefore, it was determined that a 2-D analysis is sufficient for obtaining heating rates for this run. It was also desirable to use the inverse method since it yields time-invariant heat transfer coefficients. Therefore, 2-D inverse finite volume analysis was used for the rest of the study. The comparison of 1-D and 2-D inverse finite volume results for the longitudinal positions of x/L_x of 0.25 and 0.5 are shown in

Figs. 14.a and 14.b, respectively. There is no significant difference between 1-D and 2-D results in the regions without vortices, regions with almost uniform temperatures ($0 \leq y/L_y \leq 0.2$; $0.8 \leq y/L_y \leq 1.0$). There is significant difference between the 1-D and 2-D predicted heating rates in the region with vortices present ($0.2 \leq y/L_y \leq 0.8$). The 1-D results under-predict the 2-D results at the peak heating locations, the center of vortex locations, and over-predict the 2-D results in the cooler region between two adjacent peaks. Lateral heat conduction smears the surface temperature distribution in regions with sharp heating gradients; heat gets transferred from the higher temperature areas (peaks) at vortex locations to the lower temperature areas between adjacent vortices (valleys), causing reduction of temperature at the peak and increase of temperature at the valleys. When 1-D heat transfer is utilized with the measured temperature distributions, the predicted heating rates are lower at the peaks and higher at the valleys. Multidimensional, in this case 2-D, heat transfer analysis can capture gradients better since it accounts for lateral heat conduction. The difference between heating rates calculated using 1-D and 2-D methods along the y axis at longitudinal positions of x/L_x of 0.25 and 0.5 are shown in Figs. 15.a and 15.b, respectively. There is a nominal ±5% difference between 1-D and 2-D results in the regions with almost uniform temperatures ($0 \leq y/L_y \leq 0.2$; $0.8 \leq y/L_y \leq 1.0$). This is due to inherent noise in the temperature data and how the noise gets amplified differently using the two techniques. But in the region where vortices are present ($0.2 \leq y/L_y \leq 0.8$), there is a distinct and significant difference between 1-D and 2-D results. The 1-D method under-predicts and over-predicts the 2-D results at the peaks and valley between –15% and +20%, respectively. A contour plot of the corresponding non-dimensionalized convective heat transfer coefficients calculated using the inverse 2-D finite volume technique is shown in Fig. 16.

Sharper definition of localized heating rates are evident from the 2-D results in Fig. 16 compared to the 1-D results presented in Fig. 12.

In summary, it was shown that in regions with significant spatial temperature variations 1-D heat transfer analysis could results in under-predicting and over-predicting heating rates by as much as 20% compared to 2-D analysis, and that multidimensional heat transfer techniques are necessary to predict the heating rates.

Concluding Remarks

Global transient surface temperatures were measured using an infrared thermographic technique on a 0.333-scale model of the Hyper-X forebody in the Langley Research Center 20-Inch Mach 6 Air tunnel. In these tests the effectiveness of vortices generated via gas injection for initiating hypersonic transition on the Hyper-X forebody were investigated. An array of streamwise-orientated heating striations were generated and visualized downstream of the gas injection sites. The striation patterns were attributed to the development of embedded boundary layer vortices. The use of multi-dimensional numerical finite volume techniques for calculating aeroheating rates from measured global surface temperatures was investigated. Both direct and inverse finite volume techniques were investigated and compared with the 1-D semi-infinite method.

In regions without significant spatial temperature gradients, 1-D techniques were sufficient for calculating aeroheating rates, provided that the correct initial temperature conditions were used. It was found that using the standard "pre-run" image data compared to the data at the beginning of injection of model in to the tunnel could results in significant errors. The use of time correction with 1-D semi-infinite results did not produce satisfactory results for this low heating test on a slender body. Even though the 1-D semi-infinite method produced satisfactory results, but it cannot be extended to multi-dimensional cases and can not incorporate radiation heat loss from the surface which could become at higher surface temperatures. The finite volume techniques can easily be extended to multidimensional cases and can incorporate radiation heat loss at the surface used for calculating aeroheating rates.

In regions with sharp temperature gradients due to the striation patterns 2-D finite volume techniques were necessary to more accurately capture heating rates gradients. The use of the one-dimensional technique resulted in heating rate differences of ±20% compared to 2-D technique in the calculated heating rates in the vicinity of vortices because it did not account for lateral heat conduction in the model.

Acknowledgements

This experimental effort was accomplished with the help of many dedicated individuals, a few of which are mentioned here. Testing was accomplished with the support of G. Gleason, R. Hatten, H. Stotler, K. Hollingsworth, and R. Merski.

References

1. Miller, C. G. III, "Comparison of Thin-Film Resistance Heat-Transfer Gages with Thin-Skin Transient Calorimeter Gages in Conventional Hypersonic Wind Tunnels," NASA TM-83197, December 1981.

2. Merski, N. R., "Global Aeroheating Wind-Tunnel Measurements Using Improved Two-Color Phosphor Thermography Method," *Journal of Spacecraft and Rockets*, Vol. 36, No. 2, 1999, pp. 160-170.
3. Puram, C. K., Daryabeigi, K., and Burkett, C. G. Jr., "Measurement of Steady and Unsteady Temperatures Using Infrared Thermography," *Fundamental Experimental Measurements in Heat Transfer*, ASME HTD-Vol. 179, 1991, pp. 23-29.
4. Daryabeigi, K., "Global Surface Temperature/Heat Transfer Measurements Using Infrared Imaging," AIAA 92-3959, July 1992.
5. De Luca, L., Cardone, G., and Carlomagno, G. M., "Experimental Investigation on Goertler Vortices in Hypersonic Flow," *Computational Methods and Experimental Measurements VI,* Vol. 1: Heat and Fluid Flow, Computational Mechanics Publications, Southampton, 1993, pp. 413-427.
6. Throckmorton, D. A., Zoby, E. V., Duvant, J. C., and Myrick, D. L., "Shuttle Infrared Leeside Temperature Sensing (SILTS) Experiment – STS-28 Preliminary Results," AIAA 90-1741, June 1990.
7. Blanchard, R. C., Anderson, B. P., Welch, S. S., Glass, C. E., Berry, S. A., Merski, N. R., Banks, D. W., Tietjen, A., and Lovern, M., "Shuttle Orbiter Fuselage Global Temperature Measurements from Infrared Images at Hypersonic Speeds," AIAA 2002-4702, August 2002.
8. Cook, W. J., and Felderman, E. J., "Reduction of Data from Thin Film Heat Transfer Gages: A Concise Numerical Technique," *AIAA Journal*, Vol. 4, No. 3, 1966, pp. 561-562.
9. Hollis, B. R., "User's Manual for the One-Dimensional Hypersonic Aero-Thermodynamic (1DHEAT) Data Reduction Code," NASA CR 4691, August 1995.

10. Daryabeigi, K., Huebner, L. D., “Heating Rate Measurements in Hyper-X Wing Gap,” NASA TM-2002-211740, July 2002.

11. Walker, D. G., Scott, E. P., and Nowak, R. J., “Estimation Methods for Two-Dimensional Conduction Effects of Shock-Shock Heat Fluxes,” *Journal of Thermophysics and Heat Transfer*, Vol. 14, No. 4, 2000, pp. 533-539.

12. Berry, S. A., Auslender, A. H., Dilley, A. D., and Calleja, J. F., “Hypersonic Boundary-Layer Trip Development for Hyper-X,” *Journal of Spacecraft and Rockets*, Vol. 38, No. 6, pp. 853-864, 2001.

13. Micol, J. R., “Langley Aerothermodynamic Facilities Complex: Enhancements and Testing Capabilities,” AIAA Paper 98-0147, January 1998.

14. Modest, M. F., *Radiative Heat Transfer*, McGraw-Hill, New York, 1993.

15. Hollis, B. R., Horvath, T. J., Berry, S. A., Hamilton, H. H. II, and Alter, S. J., “X-33 Computational Aeroheating Predictions and Comparisons with Experimental Data,” *Journal of Spacecraft and Rockets*, Vol. 38, No. 5, 2001, pp. 658-669.

16. Anderson, D. A., Tannehill, J. C., and Pletcher, R. H., *Computational Fluid Mechanics and Heat Transfer*, Hemisphere Publishing, Washington, 1984.

17. Kreith, F., and Black, W. Z., *Basic Heat Transfer*, Harper & Row Publishers, New York, 1980, p. 328.

18. Ozisik, M. N., and Orlande, H. R. B., *Inverse Heat Transfer: Fundamentals and Applications*, Taylor & Francis, New York, 2000.

19. Smith, R. H., and Scott, E. P., “2D Non-Uniform, Time Dependent, High Heat Flux Estimates Using Data from Thin Film Sensors and/or PT Measurements,” AIAA 2001-0506, January 2001.

20. Coleman, H. W., and Steele, W. G., Jr., *Experimentation and Uncertainty Analysis for Engineers*, Wiley, New York, 1989.

21. Hollis, B. R., “Experimental and Computational Aerothermodynamics of a Mars Entry Vehicle,” NASA CR-201633, December 1996, pp. 581-582.

22. Fay, J. A., and Riddell, F. R., “Theory of Stagnation Point Heat Transfer in Dissociated Air,” *Journal of The Aeronautical Sciences*, Vol. 25, No. 2, 1958, pp. 73-85.

23. Yan, X. T., “On the Penetration Depth in Fourier Heat Conduction,” AIAA 2002-2881, June 2002.

Table 1 Nominal tunnel flow conditions

Run Number	Re_∞ $\times10^6$/m	M_∞	P_{t1} MPa	T_{t1} K	H_{t1} KJ/kg	P_{t2} Mpa
70	7.34	5.94	0.864	503.4	506.9	0.027
71	7.36	5.94	0.865	503.9	506.4	0.027

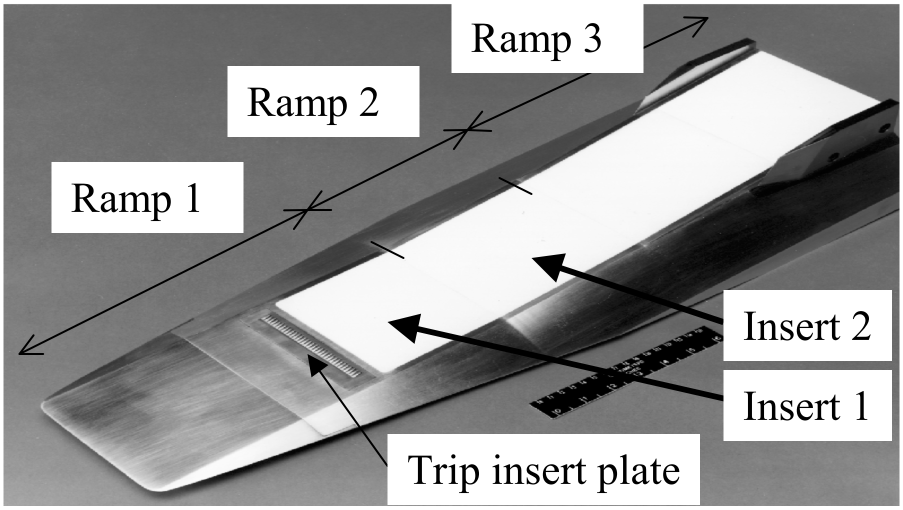

Fig. 1 Photograph of 0.333-scale Hyper-X forebody model with Macor inserts.

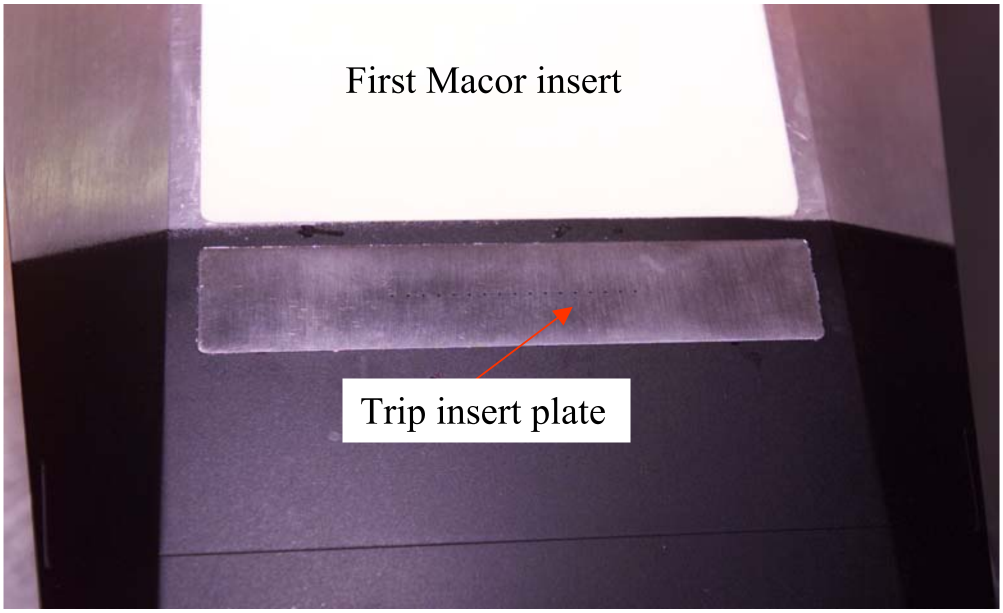

Fig. 2 Photograph of trip insert plate with 17 orifices and first Macor insert on the Hyper-X forebody model.

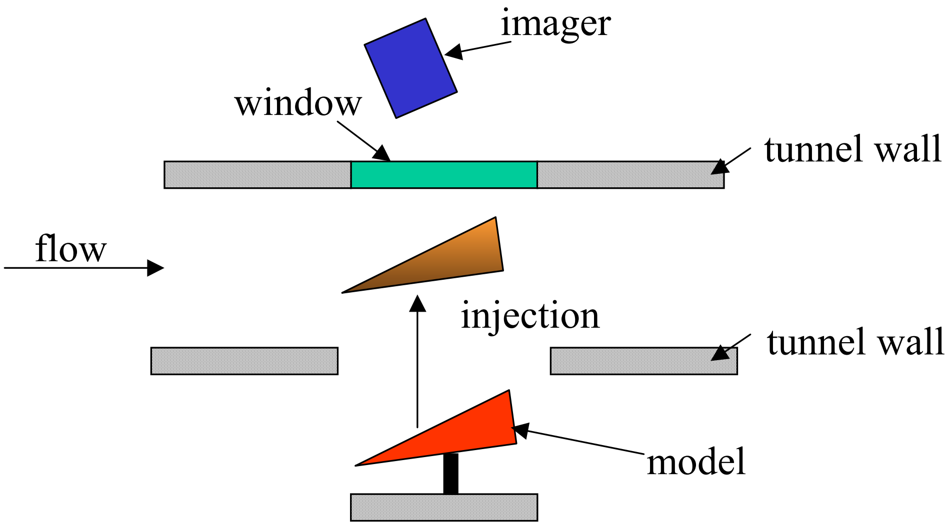

Fig. 3 Schematic of experimental set-up.

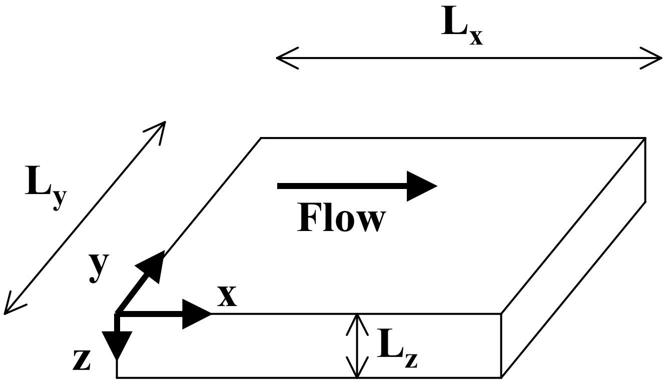

Fig. 4 Coordinate system and geometrical definitions for the first Macor insert.

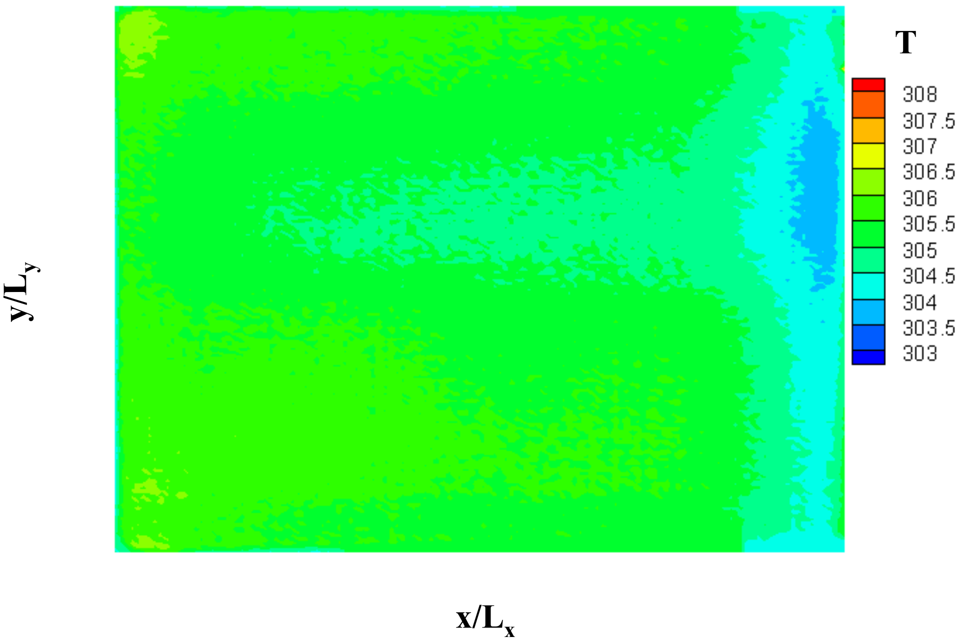

Fig. 5 Contour plot of temperature distributions at t = 4.89 s.

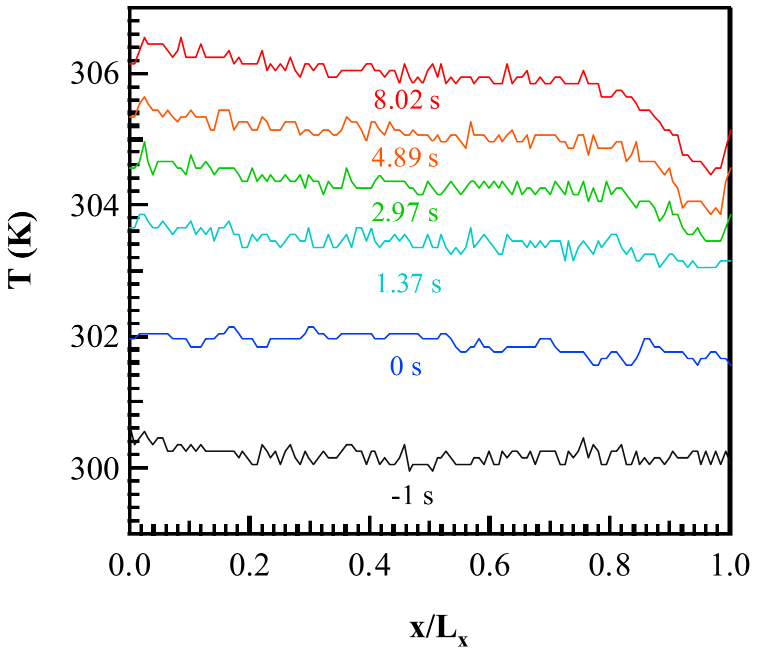

Fig. 6 Longitudinal variation of surface temperature at $y/L_y = 0.5$ at various times.

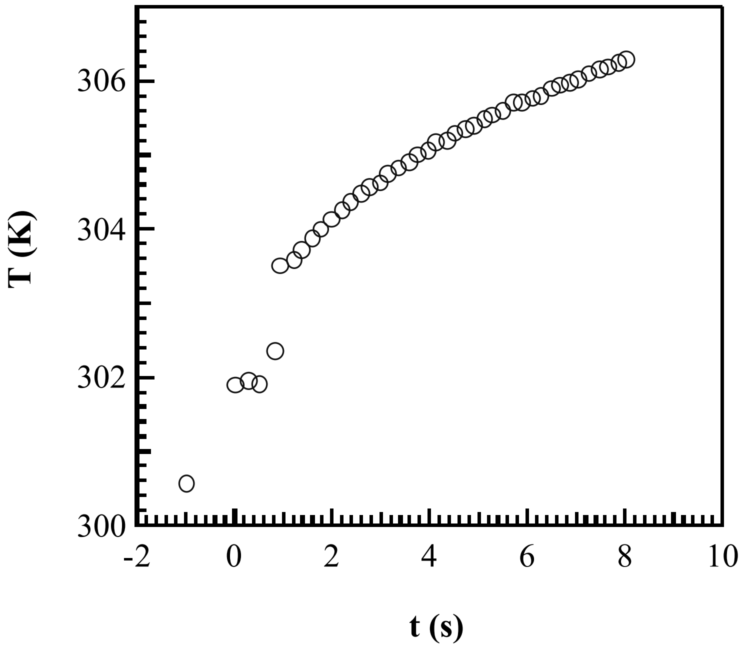

Fig. 7 Temporal variation of spanwise-averaged surface temperatures at x/L_x =0.25.

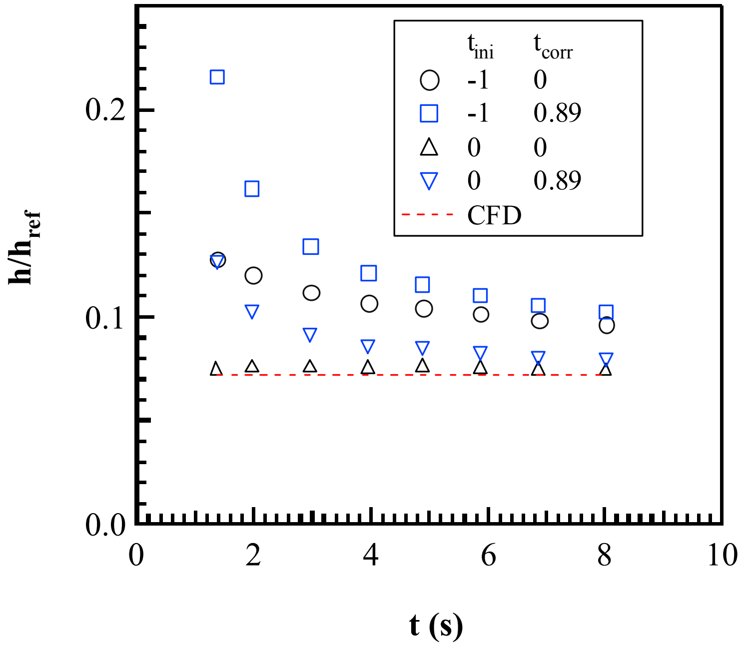

Fig. 8 Temporal variation of spanwise-averaged heating rates at x/L_x =0.25 using semi-infinite technique.

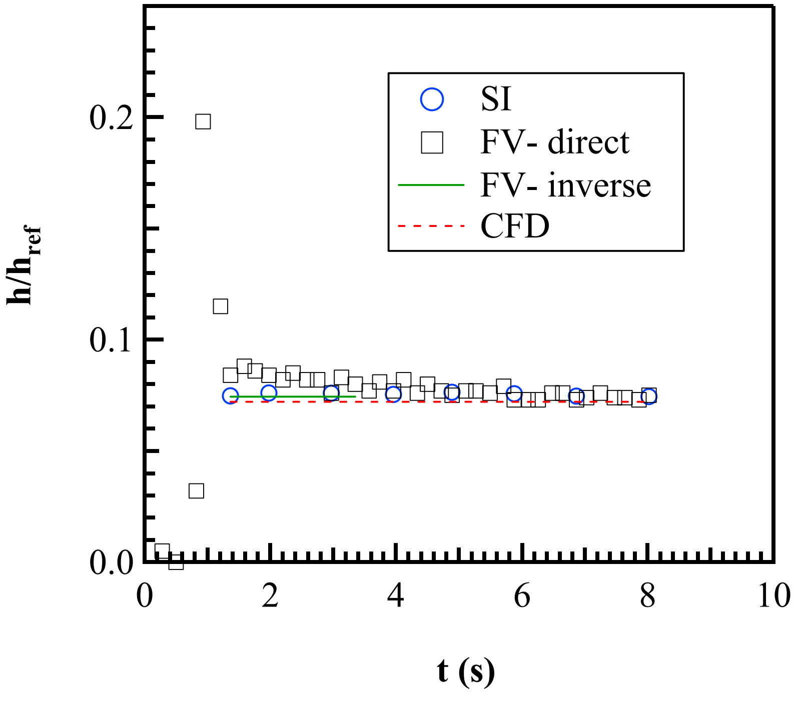

Fig. 9 Temporal variation of spanwise-averaged heating rates at x/L_x =0.25 using finite volume techniques.

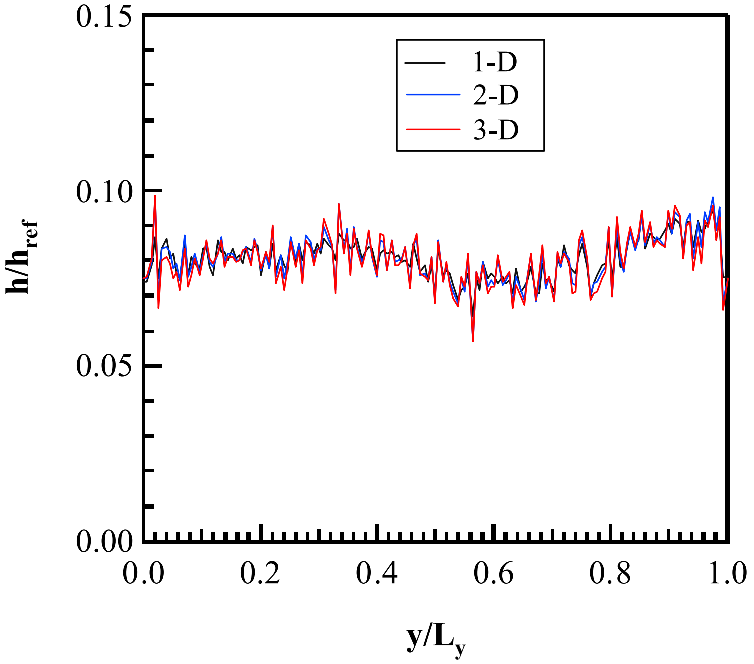

Fig. 10 Comparison of 1-D, 2-D, and 3-D direct finite volume aeroheating rates at x/L_x=0.25.

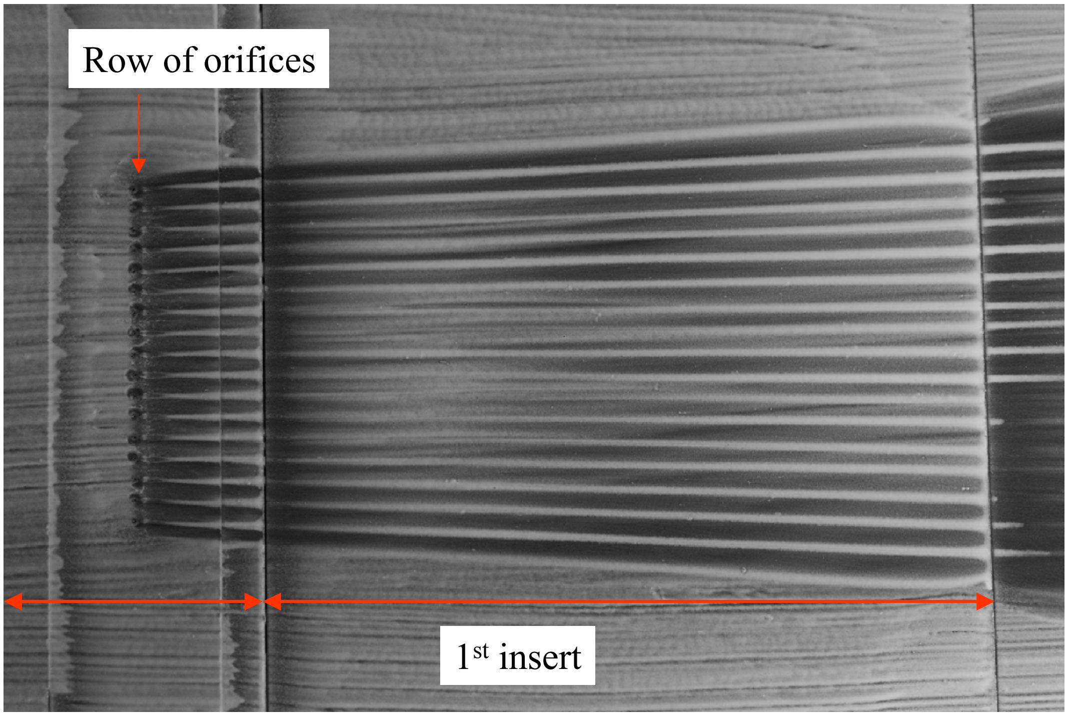

Fig. 11 Oil flow photograph for run with gas injection.

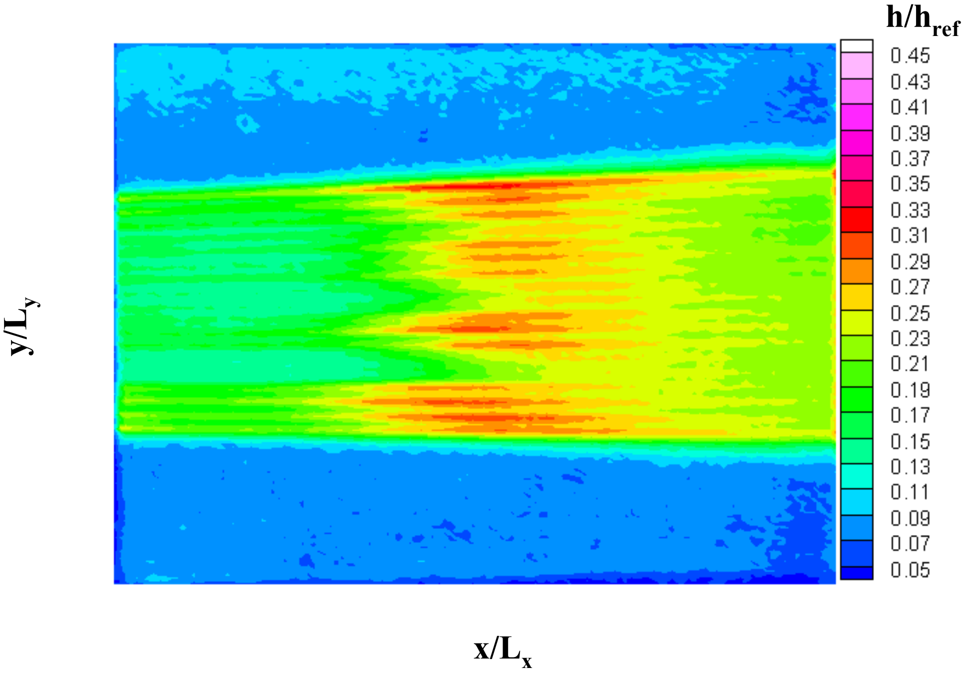

Fig 12. Spatial variation of aeroheating rates for run with gas injection using 1-D inverse finite volume technique.

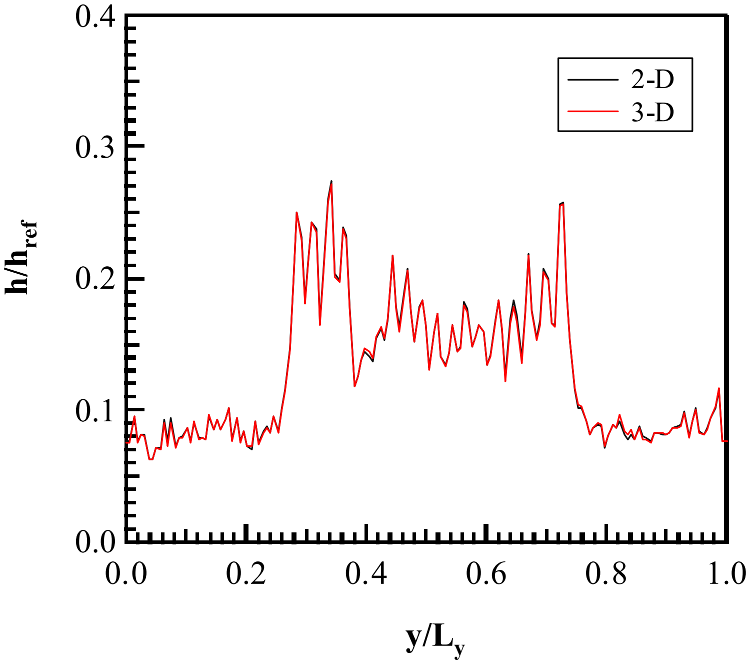

Fig. 13 Comparison of 2-D and 3-D direct finite volume aeroheating rates at $x/L_x = .25$ for run with gas injection.

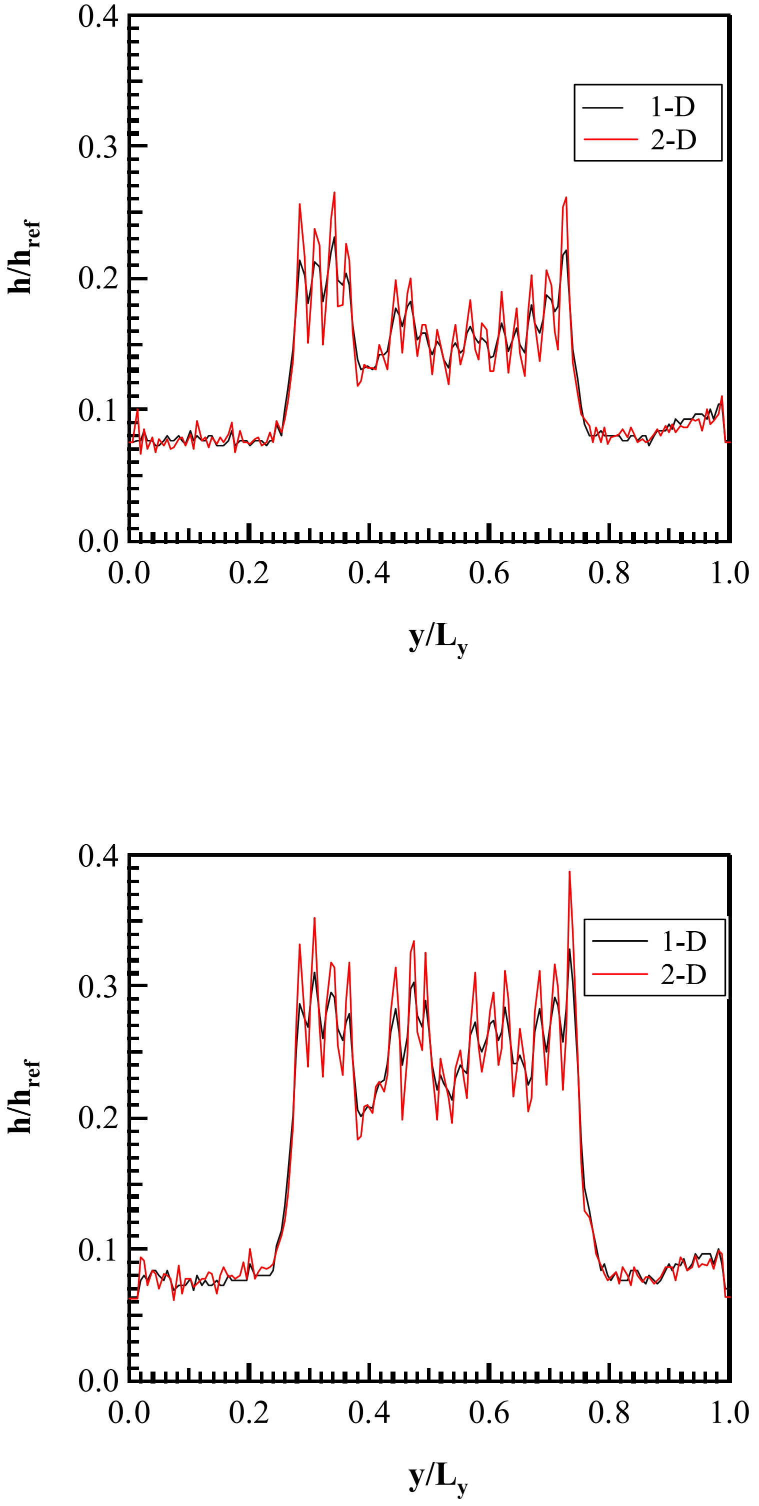

Fig. 14 Comparison of 1-D and 2-D inverse finite volume aeroheating rates for run with gas injection at x/L_x= a) 0.25, b) 0.75.

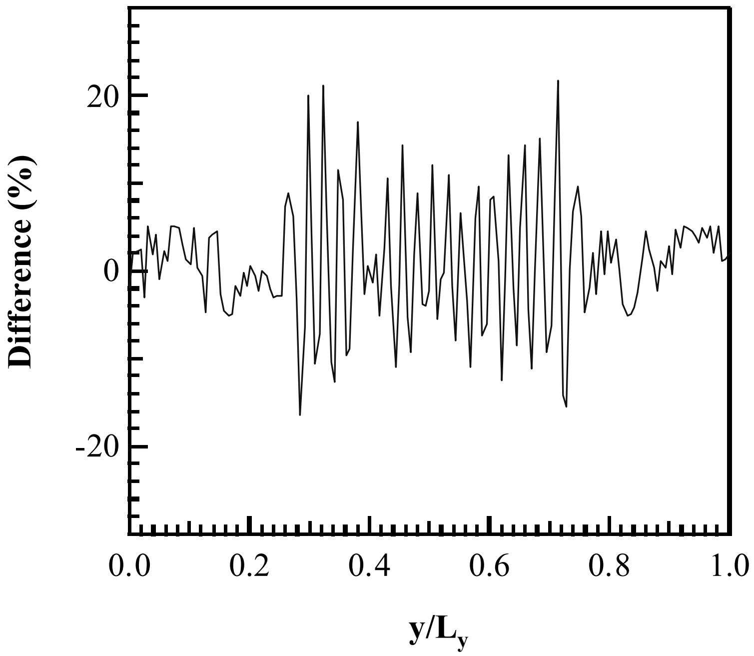

a)

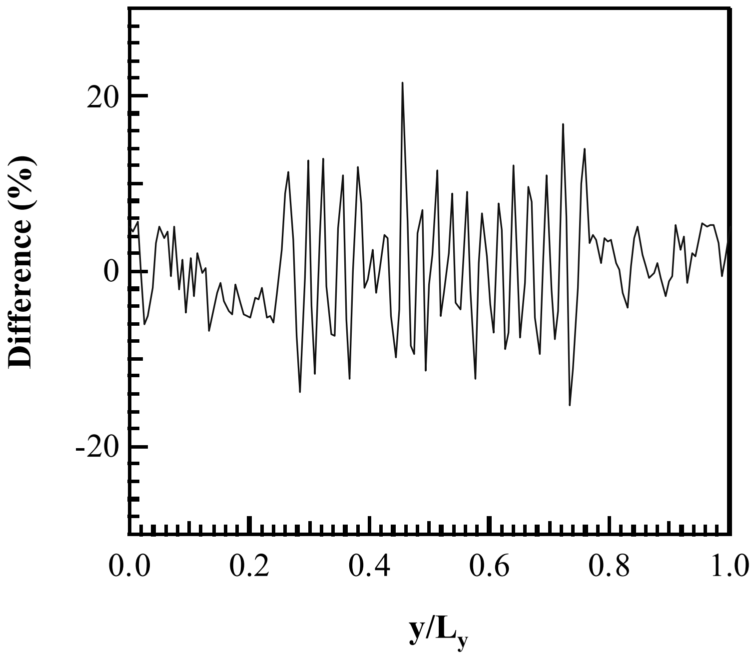

b)

Fig. 15 Relative difference between 1-D and 2-D inverse finite volume aeroheating rates for run with gas injection at $x/L_x =$ a) 0.25 b) 0.50

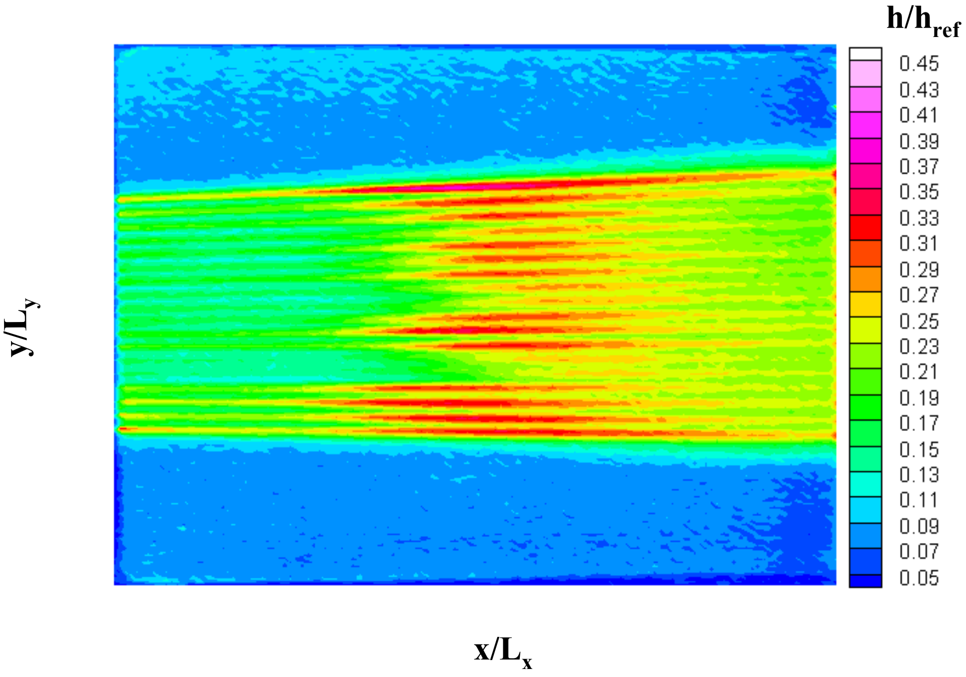

Fig 16. Spatial variation of aeroheating rates for run with gas injection using 2-D inverse finite volume technique.